CrossMark

PHANGS–JWST First Results: Stellar-feedback-driven Excitation and Dissociation of Molecular Gas in the Starburst Ring of NGC 1365?

Daizhong Liu[1] , Eva Schinnerer[2] , Yixian Cao[1] , Adam Leroy[3] , Antonio Usero[4] , Erik Rosolowsky[5] ,
J. M. Diederik Kruijssen[6] , Mélanie Chevance[6,7] , Simon C. O. Glover[7] , Mattia C. Sormani[7] , Alberto D. Bolatto[8] ,
Jiayi Sun[9,10] , Sophia K. Stuber[2] , Yu-Hsuan Teng[11] , Frank Bigiel[12] , Ivana Bešlić[12] , Kathryn Grasha[13,14] ,
Jonathan D. Henshaw[2,15] , Ashley T. Barnes[12] , Jakob S. den Brok[12] , Toshiki Saito[16] , Daniel A. Dale[17] ,
Elizabeth J. Watkins[18] , Hsi-An Pan[19] , Ralf S. Klessen[7,20] , Eric Emsellem[21,22] , Gagandeep S. Anand[23] ,
Sinan Deger[24] , Oleg V. Egorov[18] , Christopher M. Faesi[25] , Hamid Hassani[26] , Kirsten L. Larson[27] , Janice C. Lee[28,29] ,
Laura A. Lopez[3,30,31] , Jérôme Pety[32,33] , Karin Sandstrom[11] , David A. Thilker[34] , Bradley C. Whitmore[23] , and
Thomas G. Williams[2,35]

[1] Max-Planck-Institut für Extraterrestrische Physik (MPE), Giessenbachstr. 1, D-85748 Garching, Germany; dzliu@mpe.mpg.de, astro.dzliu@gmail.com
[2] Max-Planck-Institut für Astronomie, Königstuhl 17, D-69117 Heidelberg, Germany
[3] Department of Astronomy, The Ohio State University, 140 West 18th Ave, Columbus, OH 43210, USA
[4] Observatorio Astronómico Nacional (IGN), C/Alfonso XII, 3, E-28014 Madrid, Spain
[5] Department of Physics, University of Alberta, Edmonton, AB, T6G 2E1, Canada
[6] Cosmic Origins Of Life (COOL) Research DAO[36]
[7] Zentrum für Astronomie, Institut für Theoretische Astrophysik, Universität Heidelberg, Albert-Ueberle-Str 2, D-69120 Heidelberg, Germany
[8] Department of Astronomy and Joint Space-Science Institute, University of Maryland, College Park, MD 20742, USA
[9] Department of Physics and Astronomy, McMaster University, 1280 Main Street West, Hamilton, ON, L8S 4M1, Canada
[10] Canadian Institute for Theoretical Astrophysics (CITA), University of Toronto, 60 St George Street, Toronto, ON, M5S 3H8, Canada
[11] Center for Astrophysics and Space Sciences, Department of Physics, University of California, San Diego, 9500 Gilman Drive, La Jolla, CA 92093, USA
[12] Argelander-Institut für Astronomie, Universität Bonn, Auf dem Hügel 71, D-53121 Bonn, Germany
[13] Research School of Astronomy and Astrophysics, Australian National University, Canberra, ACT 2611, Australia
[14] ARC Centre of Excellence for All Sky Astrophysics in 3 Dimensions (ASTRO 3D), Australia
[15] Astrophysics Research Institute, Liverpool John Moores University, 146 Brownlow Hill, Liverpool, L3 5RF, UK
[16] National Astronomical Observatory of Japan, 2-21-1 Osawa, Mitaka, Tokyo, 181-8588, Japan
[17] Department of Physics and Astronomy, University of Wyoming, Laramie, WY 82071, USA
[18] Astronomisches Rechen-Institut, Zentrum für Astronomie der Universität Heidelberg, Mönchhofstraße 12-14, D-69120 Heidelberg, Germany
[19] Department of Physics, Tamkang University, No.151, Yingzhuan Road, Tamsui District, New Taipei City 251301, Taiwan
[20] Interdisziplinäres Zentrum für Wissenschaftliches Rechnen, Universität Heidelberg, Im Neuenheimer Feld 205, D-69120 Heidelberg, Germany
[21] European Southern Observatory, Karl-Schwarzschild-Straße 2, D-85748 Garching, Germany
[22] Univ Lyon, Univ Lyon1, ENS de Lyon, CNRS, Centre de Recherche Astrophysique de Lyon UMR5574, F-69230 Saint-Genis-Laval, France
[23] Space Telescope Science Institute, 3700 San Martin Drive, Baltimore, MD 21218, USA
[24] The Oskar Klein Centre for Cosmoparticle Physics, Department of Physics, Stockholm University, AlbaNova, Stockholm, SE-106 91, Sweden
[25] University of Massachusetts-Amherst, 710 North Pleasant Street, Amherst, MA 01003, USA
[26] Department of Physics, University of Alberta, Edmonton, AB, T6G 2E1, Canada
[27] AURA for the European Space Agency (ESA), Space Telescope Science Institute, 3700 San Martin Drive, Baltimore, MD 21218, USA
[28] Gemini Observatory/NSF's NOIRLab, 950 N. Cherry Avenue, Tucson, AZ 85719, USA
[29] Caltech/IPAC, California Institute of Technology, Pasadena, CA 91125, USA
[30] Center for Cosmology and Astroparticle Physics, 191 West Woodruff Avenue, Columbus, OH 43210, USA
[31] Flatiron Institute, Center for Computational Astrophysics, NY 10010, USA
[32] IRAM, 300 rue de la Piscine, F-38400 Saint Martin d'Hères, France
[33] LERMA, Observatoire de Paris, PSL Research University, CNRS, Sorbonne Universités, 75014 Paris, France
[34] Department of Physics and Astronomy, The Johns Hopkins University, Baltimore, MD 21218, USA
[35] Sub-department of Astrophysics, Department of Physics, University of Oxford, Keble Road, Oxford, OX1 3RH, UK

Abstract

We compare embedded young massive star clusters (YMCs) to (sub-)millimeter line observations tracing the excitation and dissociation of molecular gas in the starburst ring of NGC 1365. This galaxy hosts one of the strongest nuclear starbursts and richest populations of YMCs within 20 Mpc. Here we combine near-/mid-IR PHANGS–JWST imaging with new Atacama Large Millimeter/submillimeter Array multi-J CO (1–0, 2–1 and 4–3) and [C I] (1–0) mapping, which we use to trace CO excitation via $R_{42} = I_{CO(4-3)}/I_{CO(2-1)}$ and $R_{21} = I_{CO(2-1)}/I_{CO(1-0)}$ and dissociation via $R_{CICO} = I_{[CI](1-0)}/I_{CO(2-1)}$ at 330 pc resolution. We find that the gas flowing into the starburst ring from northeast to southwest appears strongly affected by stellar feedback, showing decreased excitation (lower R_{42}) and increased signatures of dissociation (higher R_{CICO}) in the downstream regions. There, radiative-transfer modeling suggests that the molecular gas density decreases and temperature and [CI/CO] abundance ratio increase. We compare R_{42} and R_{CICO} with local conditions across the

regions and find that both correlate with near-IR 2 μm emission tracing the YMCs and with both polycyclic aromatic hydrocarbon (11.3 μm) and dust continuum (21 μm) emission. In general, R_{CICO} exhibits $\sim$0.1 dex tighter correlations than R_{42}, suggesting C I to be a more sensitive tracer of changing physical conditions in the NGC 1365 starburst than CO (4–3). Our results are consistent with a scenario where gas flows into the two arm regions along the bar, becomes condensed/shocked, forms YMCs, and then these YMCs heat and dissociate the gas.

Unified Astronomy Thesaurus concepts: Interstellar medium (847); Molecular gas (1073); Young massive clusters (2049); Stellar feedback (1602); Starburst galaxies (1570); Interstellar line emission (844); Barred spiral galaxies (136); CO line emission (262); AGN host galaxies (2017); Dust continuum emission (412)

1. Introduction

The interplay between star formation and the interstellar medium (ISM) is a key topic in our understanding of galaxy evolution. Star formation happens in cold molecular gas (e.g., see review of Kennicutt & Evans 2012) and then young massive stars (often found in young massive clusters, or YMCs) drive energetic winds and radiation that may heat up or destroy giant molecular clouds, a process known as stellar feedback (e.g., see reviews by Chevance et al. 2020, 2022). An active galactic nucleus (AGN), if present, can also have a significant impact on the host galaxy's ISM and star formation, known as AGN feedback (e.g., see reviews by Cicone et al. 2018 and Harrison et al. 2018). Across the universe, much star formation occurs in gas-rich, turbulent, and high-surface-density regions (e.g., Tacconi et al. 2020). To understand how feedback processes operate in such intense environments, the local starburst galaxy population, and especially starbursting galaxy centers, represent key targets where we can observe the physical state of the molecular gas and the impact of stellar feedback in the greatest detail.

Thanks to high-resolution optical, e.g., LEGUS (Calzetti et al. 2015), PHANGS–HST (Lee et al. 2022), PHANGS–MUSE (Emsellem et al. 2022), MAD (Erroz-Ferrer et al. 2019), and TIMER (Gadotti et al. 2019), and millimeter-wave imaging, e.g., NUGA (Combes et al. 2019), PHANGS–ALMA (Leroy et al. 2021a), and GATOS (García-Burillo et al. 2021), we have made great strides in understanding the interplay of molecular gas, star formation, and stellar feedback in normal galaxy disks, e.g., feedback timescales (Grasha et al. 2018; Kruijssen et al. 2019; Chevance et al. 2020; Kim et al. 2022; Pan et al. 2022), pressure and turbulence (Sun et al. 2020; Barnes et al. 2021, 2022), outflows of AGNs (Audibert et al. 2019; García-Burillo et al. 2021; Saito et al. 2022a, 2022b), to name a few. However, the nuclear starbursts, which contain a significant to dominant fraction of a host galaxy's star formation and especially the most massive ($M_\star \gtrsim 10^6 M_\odot$) YMCs, are still far from being well understood.

NGC 1365 is among the most actively star-forming local galaxies (SFR = 16.9 $M_\odot$ yr^{-1}; Leroy et al. 2021a) and hosts the richest populations of YMCs in the local $\sim$20 Mpc universe (Kristen et al. 1997; Galliano et al. 2008; Whitmore et al. 2023). At a distance of 19.57 $\pm$ 0.78 Mpc (1″ = 95 pc; Anand et al. 2021a, 2021b), its nuclear starbursting ring ($R \sim$ 1.8 kpc; Schinnerer et al. 2023) is fed by gas flowing inward along bar lanes of its well-known 17 kpc long stellar bar (Lindblad 1999). An optical/radio/X-ray AGN is also well known at its center (e.g., Veron et al. 1980; Turner et al. 1993; Morganti et al. 1999; Fazeli et al. 2019). Based on the first data of PHANGS–JWST (Lee et al. 2023), 37 $M_\star \gtrsim 10^6 M_\odot$ and age $\lesssim$ 10 Myr YMCs are found within the central $\sim$3 kpc $\times$ 2.5 kpc area (Whitmore et al. 2023), more numerous than in any other galaxy within $\sim$20 Mpc.

In this work, we utilize the first PHANGS–JWST mid-IR imaging along with new and archival Atacama Large Millimeter/submillimeter Array (ALMA) multi-J (1–0, 2–1, and 4–3) CO and [C I] (1–0) line mapping to assess how tracers of CO excitation, dissociation, and other molecular gas properties relate to the location and likely evolution of embedded YMCs in this rich inner region of NGC 1365.

The spectral line energy distribution (SLED) of CO is a powerful tool to constrain gas temperature and density (e.g., Goldreich & Kwan 1974; Israel et al. 1995; Bayet et al. 2004, 2006; Papadopoulos et al. 2007, 2010; Greve et al. 2014; Kamenetzky et al. 2014; Zhang et al. 2014; Israel et al. 2015; Liu et al. 2015; Rosenberg et al. 2015; Kamenetzky et al. 2016, 2017). The CO (4–3) transition has more than an order of magnitude higher critical density and upper-level energy ($E_{u=4}/k_B$ = 55.32 K, $n_{crit.} \sim 4 \times 10^4$ cm^{-3}; Meijerink et al. 2007) than the ground 1–0 transition ($E_{u=1}/k_B$ = 5.53 K, $n_{crit.} \sim 3 \times 10^3$ cm^{-3}).[37] Therefore, a higher $R_{41} \equiv I_{CO(4-3)}/I_{CO(1-0)}$ line ratio generally means a higher density and temperature of gas, but the actual shape of the CO SLED (e.g., traced by both a mid-J ratio $R_{42} \equiv I_{CO(4-3)}/I_{CO(2-1)}$ and a low-J ratio $R_{21} \equiv I_{CO(2-1)}/I_{CO(1-0)}$) is important to distinguish the effects of changing density, temperature, and other ISM properties (e.g., turbulent line width) that may relate to the stellar feedback.

Meanwhile, the C I offers an additional potential diagnostic on the feedback affecting the dissociation of CO. C I originates from a thin dissociation layer in photon-dominated regions (Langer 1976; de Jong et al. 1980; Tielens & Hollenbach 1985a, 1985b; Hollenbach et al. 1991) exposed to the UV radiation of H II regions (Hollenbach & Tielens 1997; Kaufman et al. 1999; Wolfire et al. 2022). Cosmic rays and X-rays from YMCs and AGNs, known as the cosmic-ray dominated regions (Papadopoulos 2010; Papadopoulos et al. 2011, 2018) and X-ray dominated regions (XDRs; Maloney et al. 1996; Meijerink & Spaans 2005; Meijerink et al. 2007; Wolfire et al. 2022), respectively, can drastically increase C I abundances and lead to a high C I/CO line ratio (R_{CICO}; Israel et al. 2015; Salak et al. 2019; Izumi et al. 2020).

Because embedded YMCs and AGNs exert intense radiative and mechanical feedback, they should in principle have a strong effect on the surrounding gas, which should manifest as observable variations in the CO SLED and the C I/CO ratios. However, isolating the effects of this feedback is challenging due to the lack of high-resolution, multi-J CO and C I observations and high-resolution, high-sensitivity mid-IR imaging in the past. Therefore, in this Letter, we use the new JWST+ALMA data and present the first multi-J CO and C I + embedded YMC study to trace the molecular gas properties and

---

[37] Although practically these lines can be moderately excited and detectable even at lower densities (e.g., Scoville 2013; Shirley 2015).

feedback in the bar-fed central starbursting environment in NGC 1365.

2. Observations and Data

2.1. JWST Observations

Full descriptions of the PHANGS–JWST observations (Program ID: 02107; PI: J. Lee) are given by Lee et al. (2023). We provide a brief summary of the observations and processing used for NGC 1365 here. The galaxy was observed during two Near Infrared Camera (NIRCam) and four Mid-Infrared Instrument (MIRI) visits. The resulting NIRCam mosaic covers the central $\sim 4'.6 \times 2'.9$ (26.2 × 16.5 kpc) and the MIRI mosaic covers $\sim 3'.8 \times 2'.6$ (21.6 × 14.8 kpc). The NIRCam F200W, F300M, and F360M filters cover primarily the stellar continuum. The MIRI F1000W and F2100W filters primarily cover dust continuum imaging. In addition, the NIRCam F335M and MIRI F770W and F1130W filters recover mostly emission associated with polycyclic aromatic hydrocarbon (PAH) bands in addition to an underlying stellar and dust continuum. Hereafter, we refer to the bands by their corresponding wavelengths: 2 μm for F200W, 11.3 μm for F1130W, and 21 μm for F2100W.

We use PHANGS–JWST internal release versions "v0p4p2" for NIRCam and "v0p5" for MIRI. Lee et al. (2023) describe the data reduction used for these first results, including modifications to the default JWST pipeline[38] parameters, our customized $1/f$ noise reduction (destriping) and background subtraction for the NIRCam images, the subtraction of MIRI "off" images, and how we set the absolute background level in the MIRI images.

JWST's high sensitivity results in saturation of pixels on top of the AGN and the brightest star-forming complexes. In this work, because we convolve the JWST images to the 3''5 resolution of CO (4–3) and [C I] (1–0) lines, the saturation of brightest emission needs to be fixed. Here we use a point-spread function (PSF) curve-of-growth analysis to match the unsaturated outskirts of each bright saturated spot, i.e., the center of NGC 1365 (where the AGN is located) and the three bright star-forming complexes to the north.

Next, these images are PSF-matched to our common resolution of 3''5, corresponding to the ALMA CO (4–3) beam in this work. We use the WebbPSF software to generate the PSFs and the photutils software to create convolution kernels (with fine-tuned TopHatWindow). The images are then resampled with the reprojection software in Python to the same world coordinate system and pixel scale.

2.2. ALMA Observations of CO (1–0), (2–1) and (4–3), and [C I] (1–0)

We have obtained new ALMA Atacama Compact Array (ACA; 7 m) Band 8 observations (program 2019.1.01635.S; PI: D. Liu) that map the CO (4–3) and [C I] (1–0) from the inner part of NGC 1365. The CO (4–3) observations at 458.53 GHz cover the inner $75'' \times 22''$ (7.3 × 2.1 kpc^2) using a 19-pointing mosaic and on-source integration time of ~ 1 hr and had $T_{\rm sys} \sim 550$ K. The [C I] (1–0) observations at 489.48 GHz covered the same area using a 23-pointing mosaic and an on-source integration time of ~ 8 hr with $T_{\rm sys} \sim 500$–1000 K. The raw data were reduced using the standard ALMA calibration

pipeline with the CASA software (the CASA Team et al. 2022).

We also reduced archival ALMA 12 m+7 m observations of CO (1–0) (2015.1.01135.S; PI: F. Egusa; 2017.1.00129.S; PI: K. Morokuma) and 12 m+7 m observations of CO (2–1) (2013.1.01161.S; PI: K. Sakamoto), including the CO (1–0) and (2–1) total power (TP) data.

After running the ALMA pipeline, we imaged and processed our data into data cubes using the PHANGS–ALMA pipeline[39] (Leroy et al. 2021b). Then we used the spectral_cube[40] software to convolve our cubes to the common beam of 3''5 matching the coarsest C I data.

The native resolution of the CO (1–0) and (2–1) data are 2''4 and 0''31, respectively. Based on the arrays used, these images have maximum recoverable scales (MRSs) of $\sim 80''$ and $40''$, respectively. Our CO (4–3) and [C I] (1–0) data have 3''4–3''5 beams and 15''–20'' MRSs. For CO (1–0) and (2–1) the short spacing is corrected with the PHANGS–ALMA pipeline using their TP data; however, other lines lack the short-spacing correction. We considered using the archival 12m-only ALMA CO(3–2) data for this galaxy but found that its poor $u - v$ coverage made it not useful in the analysis presented.

We expect only a minor percentage of missing flux for our CO (4–3) and [C I] (1–0) data (e.g., $\lesssim 25\%$). Indeed, our total CO (4–3) line luminosity within a radius $\sim 14''$ is 5.3×10^8 K km s^{-1} pc^2, which is more than half of the total Herschel/SPIRE Fourier transform spectrometer CO (4–3) luminosity within a $\sim 43''$ beam $(7.3 \times 10^9 \pm 1.2 \times 10^7$ K km s^{-1} pc^2; Liu et al. 2015), scaled to the same distance. Simulations of visibilities mimicking similar ACA Band 8 observations also reveal that the missing flux is minimal at relatively bright line emission spots ($\lesssim 10\%$; D. Liu et al. 2022).

We collapsed the data cubes into moment maps using the PHANGS–ALMA imaging and post-processing pipeline. We specifically focus on the "strict," high-confidence mask, which is constructed using a watershed algorithm with relatively high clipping values (Rosolowsky & Leroy 2006; Rosolowsky et al. 2021) and so expected to include only significant detections. We build a single common strict mask by combining the individual masks for CO (1–0), CO (2–1), CO (4–3), and [C I] (1–0), then we extracted moment maps for each line therein. The error maps are also measured from the data cube, then computed for moment maps following the standard procedures implemented in the PHANGS–ALMA pipeline. In our final moment-0 maps, the signal-to-noise ratio is 5–200 for CO (4–3), 5–100 for [C I] (1–0), and much higher, 20–250, for CO (1–0) and CO (2–1). We create line-ratio maps from every pair or lines at the best common resolution of 3''5 and use them to compute correlations and CO SLEDs.

2.3. Auxiliary Data Products and Complementary Information

We use the YMC catalog from Whitmore et al. (2023, this Issue) to determine the locations where CO and C I line fluxes are extracted and studied. It contains 37 YMCs with the Hubble Space Telescope (HST) or JWST photometry-derived masses $M_\star \sim 1 \times 10^6$–$2 \times 10^7$ $M_\odot$ and ages ~ 1–8 Myr.

We use the CO (2–1) line-of-sight decomposition and orbital time information from Schinnerer et al. (2023, this Issue) for

---

discussions relating to line velocity dispersion. Schinnerer et al. (2023) present the $0\farcs3$ resolution CO (2–1) data and decomposition of each line-of-sight spectrum into multiple Gaussian components with the ScousePy software (Henshaw et al. 2016, 2019). They find that multiple velocity components exist in the system, and individual components have a typical line width $\sigma \sim 19\,\mathrm{km\,s^{-1}}$. We use this value as the micro-turbulent line width σ for our later radiative-transfer calculation. They derive a dynamical timescale $t_{\mathrm{dyn}} \sim 20\,\mathrm{Myr}$ at $R = 5'' \approx 475\,\mathrm{pc}$, which is roughly the radius of the dynamically cold inner gas disk in this starburst ring system. This timescale is used as a context for discussion in this work.

3. Results and Discussion

3.1. Spatial and Kinematic Structure

In Figure 1 we present the ALMA and JWST data at their native resolution ($\sim 6\,\mathrm{pc}$ at $2\,\mu m$, $\sim 30\,\mathrm{pc}$ for CO (2–1), and $\sim 60\,\mathrm{pc}$ at $21\,\mu m$) and the multi-J CO and C I ratio maps at their common resolution of $3\farcs5$ ($\sim 330\,\mathrm{pc}$). We define $R_{21} = I_{\mathrm{CO(2-1)}}/I_{\mathrm{CO(1-0)}}$ to trace the low-J CO excitation, $R_{42} = I_{\mathrm{CO(4-3)}}/I_{\mathrm{CO(2-1)}}$ for the mid-J excitation, and $R_{\mathrm{CICO}} = I_{\mathrm{[CI]\,(1-0)}}/I_{\mathrm{CO(2-1)}}$ as a tentative tracer of CO dissociation.

We also label four regions in this study to facilitate the later discussion: (i) the "Northern Arm," which is where the gas flows in from northeast along the bar; (ii) the "Mid-Southwest" region, which is the downstream location of the gas coming from the Northern Arm (and we call the Northern Arm the upstream of the Mid-Southwest region); (iii) the "Southern Arm," similar to the Northern Arm, is the location of gas flowing in from the southeast along the bar; (iv) the "Mid-East" region, considered as the downstream of the Southern Arm. The Northern Arm and Mid-Southwest region both belong to the "northern bar lane" as defined in Schinnerer et al. (2023), and the Southern Arm and Mid-East region correspond to the "southern bar lane" therein. The Northern Arm alone is also emphasized as the "region 1" in Whitmore et al. (2023).

The CO emission mostly arises from the prominent starburst ring, oriented from northeast to southwest, but exhibits a highly asymmetric distribution within this ring. The $2\,\mu m$ stellar emission, which is much less affected by dust attenuation than HST optical images, reveals a more symmetric distribution than CO. We show the azimuthal profiles of the CO, 2, 11.3 and $21\,\mu m$ emission along the starburst ring in Figure 2. These profiles are measured from the radially averaged emission at each azimuthal angle θ using a common annulus at our working resolution of $3\farcs5$. Here, $\theta = 0°$ corresponds to the receding side of the major kinematic axis with a position angle (PA) of $220°$, and $\theta = 180° (-180°)$ to the approaching side. All azimuthal profiles show a peak at $\theta_{\mathrm{max}} \sim 150°$, corresponding to the Northern Arm region. The $2\,\mu m$ profile shows the least azimuthal variation, of about 50% (with a maxima-to-minima ratio of 1.9), whereas the other three profiles show large variations $\sim 80\%$–95%, with a maxima-to-minima ratio of 8.5, 6.0, and 19.4, for CO, 11.3 μm, and $21\,\mu m$, respectively.

The Northern Arm peak ($\theta \sim 150°$) in the azimuthal profiles mainly consists of three extremely massive star clusters, YMC 29, 33, and 28, corresponding to Galliano et al.'s (2005, 2008) mid-IR ID M4, M5, and M6, and Sandqvist et al.'s (1995) radio 20 cm/6 cm ID D, E, and G, respectively.

In Figure 3 we show the distribution of YMCs on the HST RGB and JWST $2\,\mu m$ image, and indicate the dust lanes by two pairs of curved arrows. The CO (2–1) emission contours broadly match the dust lanes in the Northern and Southern Arm regions but appear to be narrow at the edge of dust lanes. Such dust lanes in barred galaxies are usually seen as a result of dissipative processes in the gaseous component, and the widely accepted view is that they delineate shocks in the interstellar gas (e.g., see reviews by Sellwood & Wilkinson 1993, Buta & Combes 1996, and Lindblad 1999; see also Pastras et al. 2022 for detailed simulations).

In addition to the gas and dust lanes, we also highlight in Figure 3 the YMCs younger than $\sim 3\,\mathrm{Myr}$ and more attenuated than $A_V \sim 8$ mag with cyan squares and yellow stars, respectively. The majority of the most massive, young, and attenuated YMCs sit in the Mid-Southwest and Mid-East regions.

The multi-J CO and C I line-ratio maps exhibit a significant asymmetry, as well. The Northern Arm region shows a factor of 1.5–2× higher excitation and dissociation than other regions, as traced by R_{42} and R_{CICO}. In particular, the R_{42} and R_{CICO} peaks coincide with the YMC ID 29 in the Northern Arm, which also corresponds to the mid-IR source M4 in Galliano et al. (2005, 2008). It has the highest CO excitation ($R_{42} \sim 0.51 \pm 0.01$, $R_{21} \sim 0.92 \pm 0.01$) and shows the most signs of dissociation ($R_{\mathrm{CICO}} \sim 0.17$). The distributions of low-J excitation, R_{21}, mid-J excitation, R_{42}, and our photodissociation tracer, R_{CICO}, also appear distinct from one another. R_{21} shows a more symmetric, smooth distribution than the other two line ratios. The $\log R_{21}$ is above -0.1 in most regions, indicating that CO (2–1) is almost thermalized in the regions we study. The R_{42} and R_{CICO} ratios have much larger dynamical ranges, and both peak in the Northern Arm. However, R_{42} is depressed whereas R_{CICO} is enhanced in the Mid-Southwest region, and their trends are the opposite in the Southern Arm region.

The molecular gas has complex, rapidly changing kinematics in these regions. Panels (d) and (g) in Figure 1 show the line-of-sight velocity and line velocity dispersion maps. The Northern and Southern Arm regions correspond to locations where molecular gas flows inward along the bar. The dissipative gas flow in such a strong bar potential can trigger shocks at the leading edge of the bar, appearing as dust lanes following the orbital skeleton (e.g., Athanassoula 1992; Sellwood & Wilkinson 1993; Buta & Combes 1996; Lindblad 1999; Pastras et al. 2022; Sellwood & Masters 2022; see also Figure 1 of Maciejewski et al. 2002). In the Southern Arm, the enhanced R_{42}, nonenhanced R_{CICO}, lack of YMCs, and elevated velocity dispersion $\sigma \sim 50\,\mathrm{km\,s^{-1}}$ (Figure 1(g)) may suggest a scenario wherein shocks triggered at the edge of dust lanes are compressing the gas and hence highly exciting the mid-J CO, but not leading to significant CO dissociation or higher C I abundance in this region. However, in other cases, e.g., the Northern Arm, when the gas is so dense and even fragments to trigger intensive star formation and hence stellar feedback, the effect of shocks can be mixed with the stellar-feedback effect. Future observations of shock tracers like SiO or HNCO for less-destructive shocks (e.g., Usero et al. 2006; García-Burillo et al. 2010; Meier et al. 2015; Kelly et al. 2017) will be the key to shed light on this shock scenario.

In panel (d) of Figure 1 we also highlight the well-known ionized gas outflow (Phillips et al. 1983; Sandqvist et al. 1995; Hjelm & Lindblad 1996; Lindblad 1999; Sakamoto et al. 2007;
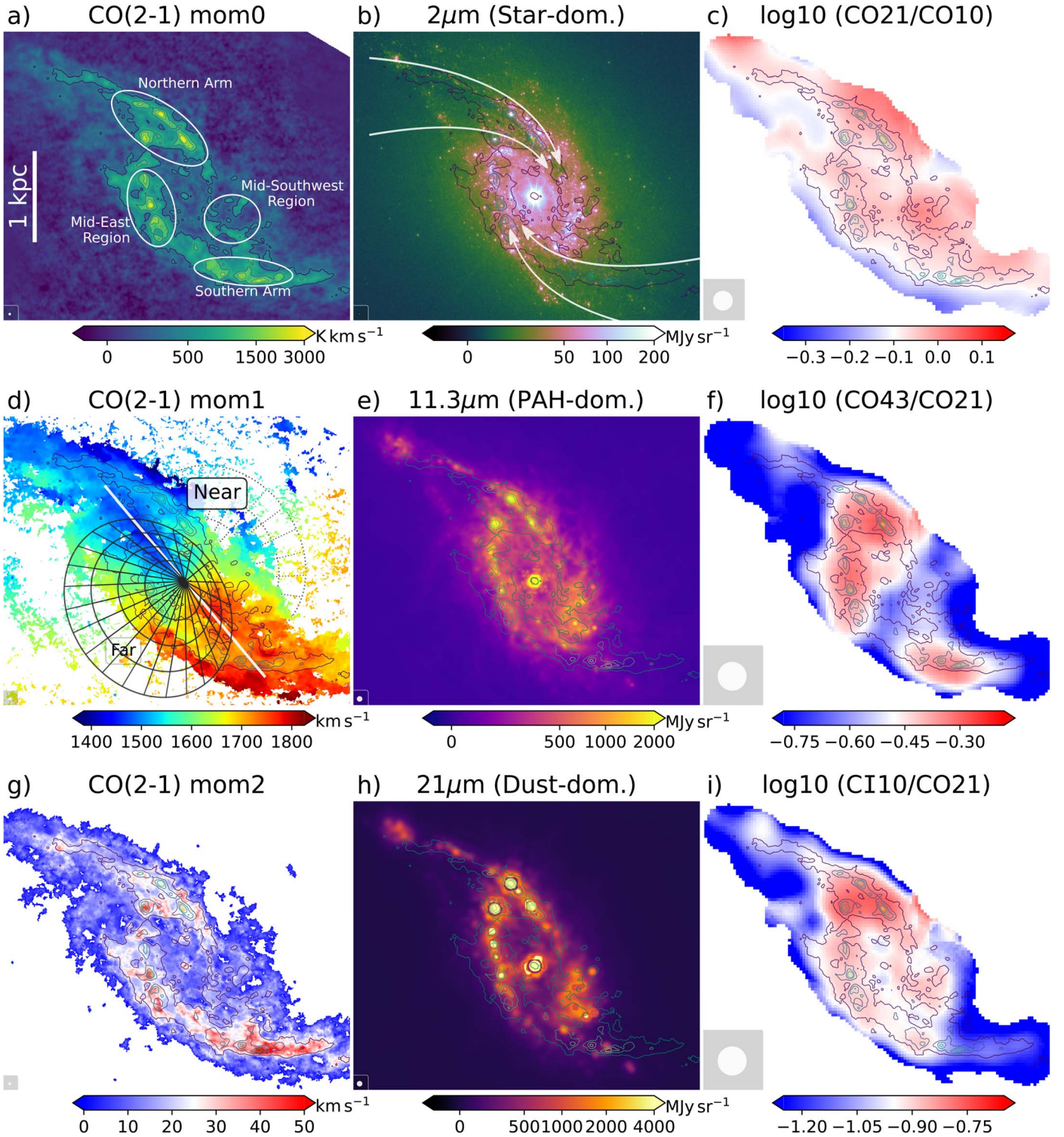
Figure 1. ALMA and JWST images of NGC 1365. Left column (*a*), (*d*), (*g*): native-resolution ($0\farcs3$) ALMA CO (2–1) integrated intensity (mom0), line-of-sight velocity (mom1), and velocity dispersion (mom2); see also Schinnerer et al. (2023). Middle column (*b*), (*e*), (*h*): JWST stellar-continuum-dominated NIRCam 2 μm, PAH-dominated MIRI 11.3 μm, and dust-continuum-dominated MIRI 21 μm, all at native resolutions; see also Whitmore et al. (2023). Right column (*c*), (*f*), (*i*): ratio maps in logarithmic scale for $R_{21} = I_{\mathrm{CO(2-1)}}/I_{\mathrm{CO(1-0)}}$, $R_{42} = I_{\mathrm{CO(4-3)}}/I_{\mathrm{CO(2-1)}}$, and $R_{\mathrm{CICO}} = I_{\mathrm{[CI]\,(1-0)}}/I_{\mathrm{CO(2-1)}}$ at the common resolution of $3\farcs5$ (beam is shown in bottom left). Same contours of $I_{\mathrm{CO(2-1)}}$ at 400, 1000, 1500, 2000, and 3000 K km s^{-1} are shown in all panels. The four regions mentioned in this work are highlighted in panel (*a*). The cone in panel (*d*) represents the known ionized gas outflow with a half-opening angle 50°, cone axis inclination 35°, and PA 126° (Hjelm & Lindblad 1996; see also Sandqvist et al. 1995; Lindblad 1999; Venturi et al. 2018; Gao et al. 2021) and the white line indicates the disk kinematic major axis at PA 220° (Jorsater & van Moorsel 1995; Lindblad 1999).

Lena et al. 2016; Venturi et al. 2018; Gao et al. 2021). We do not find a high R_{42} or enhanced R_{CICO} peaking at the center and extending along the outflow cone, unlike the cases of known

C I molecular outflows in AGN host galaxies (e.g., Saito et al. 2022a, 2022b, with $R_{\mathrm{CICO}} \sim 1$). This agrees with Schinnerer et al. (2023), who find no evidence for the ionized outflow to
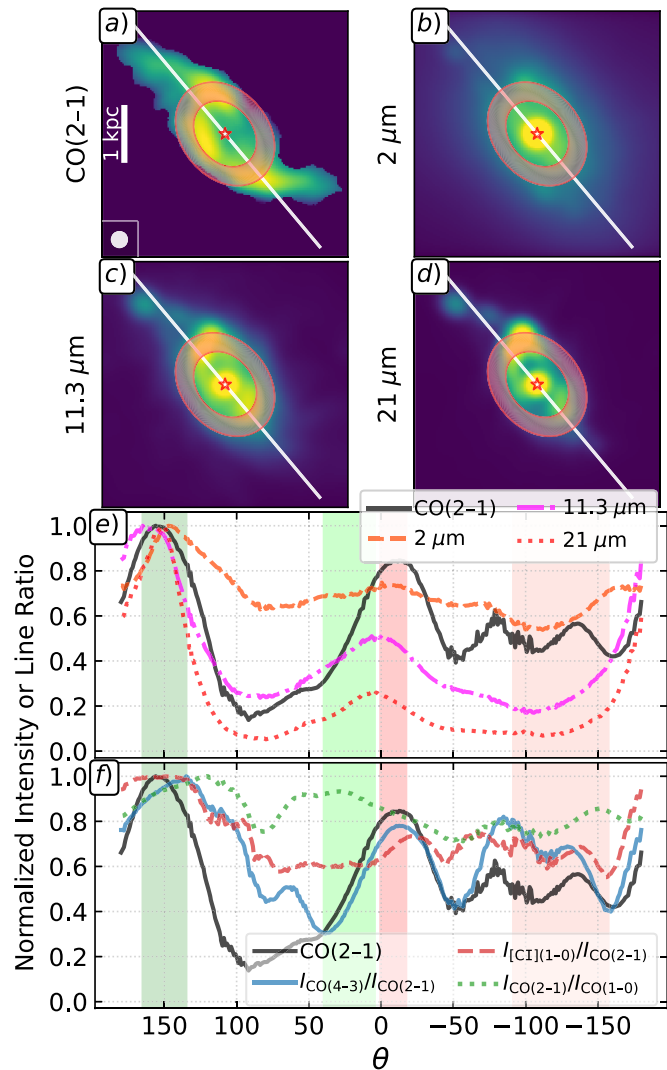
Figure 2. Panels (a)–(d) are the CO (2–1) line-integrated intensity, 2, 11.3, and 21 μm images, PSF-matched to our 3″5 resolution. A common annulus is shown in all panels with radius $=0.9 \pm 0.2$ kpc, inclination 40°, and PA 220° (white solid line; Lindblad 1999). Panels (e)–(f) show the normalized azimuthal profiles of the four upper panels and R_{42}, R_{CICO}, and R_{21} line ratios as a function of azimuthal angle θ measured from the PA of the receding side of the kinematic major axis. Dark green, light green, dark red, and light red shading represents the Northern Arm, Mid-Southwest, Southern Arm, and the Mid-East regions, respectively.

intersect the molecular gas disk, and with Combes et al. (2019), who find that this region lacks a molecular gas outflow (and instead shows evidence for inflow).

3.2. Zoom-in Views and CO and C I Excitation

We examine the aforementioned regions in more detail in Figure 4. We first draw hexagonal apertures centered on bright YMCs (Whitmore et al. 2023), CO peaks that do not coincide with a YMC (based on Figure 4, hereafter YMC-free CO peaks, labeled as CO.N1/N2 and CO.S1/S2/S3 for those in the Northern and Southern Arms, respectively), and the galaxy center, each with a 330 pc diameter. Then, we take the pixel value at the hexagon center from the 3″5 resolution moment-0 map for each line, and show their normalized CO and C I SLED in the right panels of Figure 4. The hexagons in the left panels
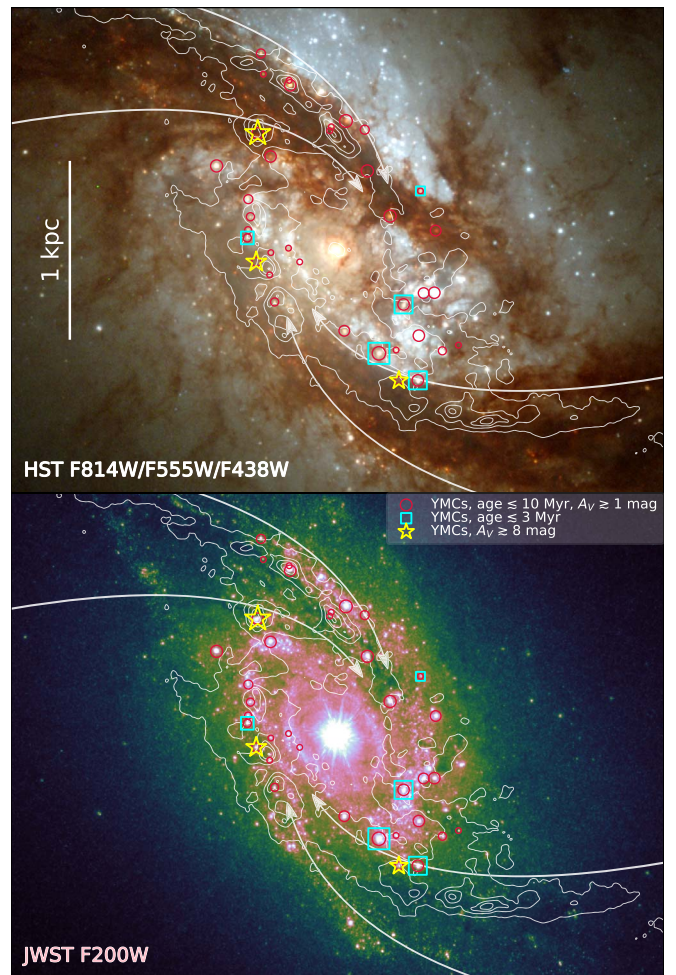
Figure 3. YMCs (Whitmore et al. 2023) overlaid on HST RGB (F814W/F555W/F438W) image (top) and JWST F200W (2 μm) image (bottom). All YMCs are shown as red circles. Symbol sizes, from smallest to largest, indicate masses from $\sim 10^{6.0} M_\odot$ to $\sim 10^{7.1} M_\odot$. Cyan squares are YMCs with an age less than ~ 3 Myr, and yellow stars are YMCs with an attenuation $A_V > 8$ mag. We show these YMCs for the context of the discussion in Section 3.1 of this work. See Whitmore et al. (2023) for the original and detailed study of these YMCs.

are then color-coded by their mid-J excitation, R_{42}. In this way we can clearly see how gas in the apertures is excited.

The most (mid-J) excited aperture is YMC 29 (M4), coinciding with the brightest CO peak in the Northern Arm, with $R_{42} = 0.50 \pm 0.01$ (and $R_{21} = 0.92 \pm 0.01$, $R_{41} = 0.46 \pm 0.01$). Its stellar age is estimated as ~ 3 Myr (with a ~ 0.4–0.6 dex uncertainty; Whitmore et al. 2023). The least (mid-J) excited aperture we analyzed is YMC 12 (M3) in the Mid-Southwest region, with $R_{42} = 0.24 \pm 0.02$. However, its low-J excitation is still quite high, with $R_{21} = 0.98 \pm 0.02$. It is also very young, with a stellar age ~ 3 Myr (with a similarly large uncertainty; Whitmore et al. 2023). Other YMCs and YMC-free CO peaks have R_{42} values in between these two extreme cases.

Based on the motion of gas along the dust lanes and starburst ring (Figures 1–3), the Northern Arm is upstream of the Mid-Southwest region, and the Southern Arm is upstream of the Mid-East region. Gas enters the system first via the Northern/Southern arms then moves to the Mid-Southwest/Mid-East regions, forming the starburst ring. Along the Northern Arm, gas moves from the less-excited CO.N2 location to the highly excited CO.N1 position. Then, in about a quarter of the orbital
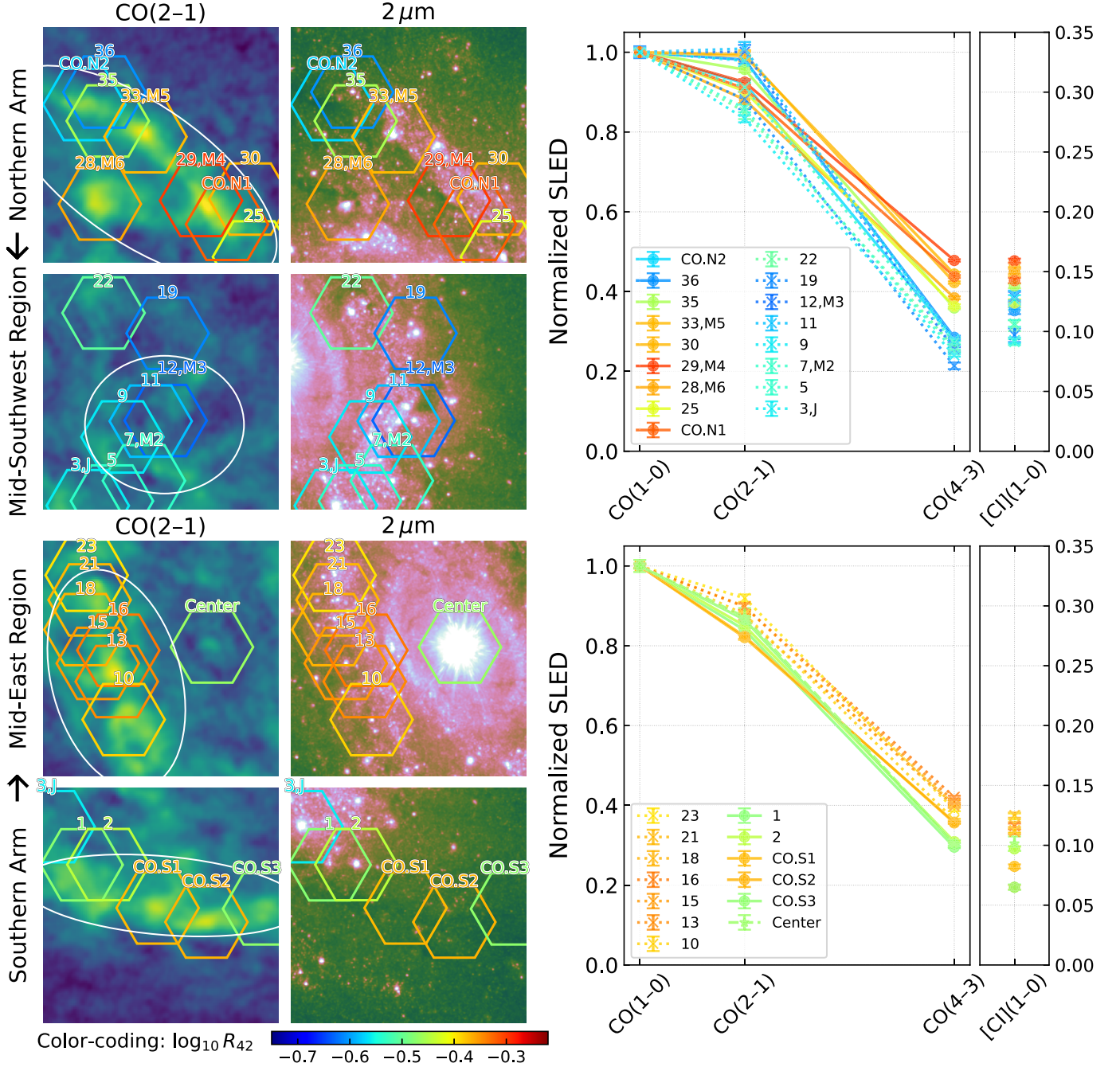
Figure 4. Left panels: CO (2–1) and 2 μm zoom-in images of the Northern Arm, Mid-Southwest, Mid-East, and Southern Arm regions (from top to bottom). Hexagons indicate YMCs identified by Whitmore et al. (2023; with numbers indicating their ID from that Letter), YMC-free CO peaks (labeled "CO.N1–N2" and "CO.S1–S3" in Northern and Southern regions, respectively, visually identified from this work), and the galaxy center. The "M2"–"M6" labels indicate YMCs that have a mid-IR counterpart from Galliano et al. (2005). The "J" label indicates that YMC 3 has a radio counterpart from Sandqvist et al. (1995). All images have the same field of view of 10″ (∼950 pc) and color scaling as in Figure 1. Hexagons have the same diameter of 3″.5 (∼330 pc). The black arrows at left indicate the upstream-to-downstream directions. Right panels: CO and C I SLEDs of the hexagons centered at YMCs or YMC-free CO peaks in the corresponding upper/lower four left image panels. Hexagons and SLEDs are color-coded by their R_{42} (see the bottom color bar). Solid and dotted lines represent upstream and downstream regions, respectively. The center's CO SLED is shown as the dashed line in the lower panel. These CO and C I SLEDs are used for the radiative-transfer modeling fitting in Section 3.2, with gas properties reported in Table 2.

time, i.e., ∼5 Myr, the gas will arrive in the Mid-Southwest region, where the CO excitation is decreasing again. It is expected that gas will move from the Mid-Southwest region toward the Southern Arm and possibly trigger collision and compression. Similarly, starting from the Southern Arm, the gas moves from CO.S3 to the CO.S2 and CO.S1 positions, then circles to the Mid-East region and heads toward the Northern

Arm. The youngest YMCs are found in these possibly colliding areas, e.g., YMC 3 (J) and YMC 28 (M6, G), which both have an age ∼1 Myr and are highlighted as yellow stars in Figure 3.[41]

---

[41] This gas colliding scenario is similar to the hypothesis of the formation of the youngest super star cluster RCW 38 in the Milky Way (Fukui et al. 2016).
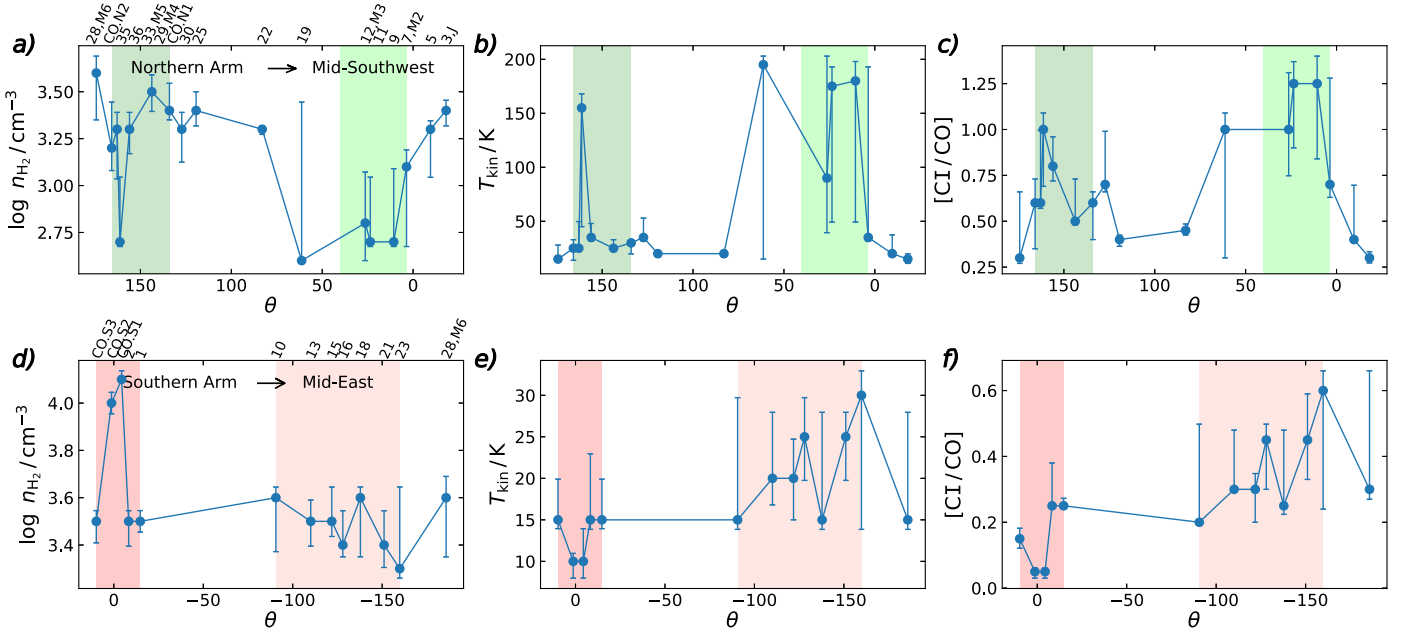
Figure 5. Non-LTE LVG model fitting results for CO and C I SLEDs in hexagon apertures (see Figure 4) in the Northern Arm to Mid-Southwest regions (upper panels) and Southern Arm to Mid-East regions (lower panels), respectively. The x-axis is the azimuthal angle starting clockwise from the PA = 220° direction, same as in Figure 2. Dark/light green and red shadings indicate the θ range of the corresponding regions. The y-axes show (from left to right) gas volume density (log n_{H_2}), kinetic temperature ($T_{\rm kin}$), and the [CI/CO] abundance ratio. Hexagon IDs are indicated at the top of the left panels at their corresponding θ. Error bars are the $\pm 1\sigma$ uncertainty from the fitting, based on MICHI2 (Liu et al. 2021; see also the Appendix). We discuss the trends of decreasing log n_{H_2} and increasing $T_{\rm kin}$ and [CI/CO] from the upstream (dark green/red, left part of each panel) to the downstream regions (light green/red, right part of each panel) in Section 3.2.

To obtain a quantitative description of the gas excitation and photodissociation along the starburst ring, we perform a non-local thermodynamic (non-LTE) large velocity gradient (LVG) radiative-transfer modeling of the CO and C I SLEDs for the YMC apertures and CO peaks to evaluate the gas density and temperature and [CI/CO] abundance ratio. We use the MICHI2 Monte Carlo fitting tool (Liu et al. 2021), with templates generated by the RADEX software (van der Tak et al. 2007) with a grid of gas kinetic temperature $T_{\rm kin} \sim 5$–200 K, H$_2$ volume density (log n_{H_2}/cm^{-3} = 2.0–5.0), [CI/CO] abundance ratio 0.05–3.0, and a fixed-line turbulent FWHM $\Delta v = 45$ km s^{-1} (matching the average CO line width of $\sigma \sim 19$ km s^{-1} inferred at 30 pc resolution; see Figure 1; Schinnerer et al. 2023), as well as a free beam-filling factor.[42] We show examples of our LVG fitting to the most-excited and least-excited YMC apertures, YMC 29 (M4) and YMC 12 (M3), respectively, in the Appendix. We find $\log(n_{H_2}/{\rm cm}^{-3}) \sim 3.50^{+0.09}_{-0.11}$ and $\sim 2.80^{+0.27}_{-0.20}$, and $T_{\rm kin} \sim 25^{+8}_{-2}$ K and $\sim 90^{+113}_{-51}$ K, respectively. Table 2 reports the best-fit parameters and 1σ uncertainties for all apertures.

In Figure 5 we present the LVG fitting results for all apertures whose CO plus C I SLEDs are shown in Figure 4. The fitted log n_{H_2}, $T_{\rm kin}$, and [CI/CO] are plotted as functions of azimuthal angle θ (see Figure 2). In the upper panels of Figure 5, θ ranges from $\sim 160°$ to $\sim 10°$, in clockwise direction, tracking the gas movement from the Northern Arm (dark green shading) to the Mid-Southwest region (light green shading). Similarly, in the lower panels of Figure 5, θ spans $\sim 0°$ to $\sim -150°$, in clockwise direction, from the Southern Arm (dark

red shading) to the Mid-East region (light red shading). We find tentative trends that log n_{H_2} is lower, $T_{\rm kin}$ is higher, and [CI/CO] is higher downstream the gas flow. The [CI/CO] ratio increases up to ~ 1.4 at the Mid-Southwest YMC 13, YMC 12 (M3), and YMC 10 locations. Such a high C I abundance relative to CO is likely due to the strong radiation field created by the YMCs in a relatively diffuse molecular gas.

Therefore, we propose a scenario where gas arriving from the dust lanes is piled up, compressed and shocked at the Arm regions, and YMCs are formed; then, gas and YMCs travel to the downstream region during about a quarter of the orbital period (a few million years); the gas may continue forming stars (clusters) on the way, but must undergo strong stellar feedback, so that it is heated and C I-enriched upon its arrival in the Mid-Southwest/Mid-East regions, as our LVG fitting results suggest.

We caution that the above picture still needs higher-resolution observational supports. The trends are only significant in the Northern Arm to Mid-Southwest side ($T_{\rm kin}$ increases from below 50 K to above 100 K and [CI/CO] increases by a factor of 2). The other side of the starburst ring from Southern Arm to Mid-East region indeed has much weaker temperature and [CI/CO] variations. The variations of n_{H_2}, $T_{\rm kin}$, and [CI/CO] along the ring are also highly nonmonotonous. We note that the environment in this starburst ring system is highly dynamic and stochastic. The density of the inflow cold gas feeding the starburst ring likely has an impact on how much the stellar feedback can affect the natal molecular gas. The Southern Arm gas density is much higher than that of the Northern Arm from our fitting, in line with the gas in the Southern Arm/Mid-East regions being more shielded and less affected by the stellar feedback.

Finally, although the galaxy center hosts a Seyfert 1.5 AGN and a prominent [O III] ionized gas outflow (Phillips et al. 1983; Sandqvist et al. 1995; Hjelm & Lindblad 1996; Lindblad 1999; Sakamoto et al. 2007; Venturi et al. 2018;

---

[42] A fixed CO abundance per velocity gradient $[{\rm CO/H_2}]/(dv/dr) = 10^{-5}$ km^{-1} s pc is also adopted (e.g., Curran et al. 2001; Weiß et al. 2007; Zhang et al. 2014; Liu et al. 2021). This leads to a nonindependent CO column density $N_{\rm CO} = [{\rm CO/H_2}] \times n_{H_2} \times \Delta v/(dv/dr)$ that has reasonable values from our fitting (log $N_{\rm CO}$/cm$^{-2} \sim 17.5$–18.7).
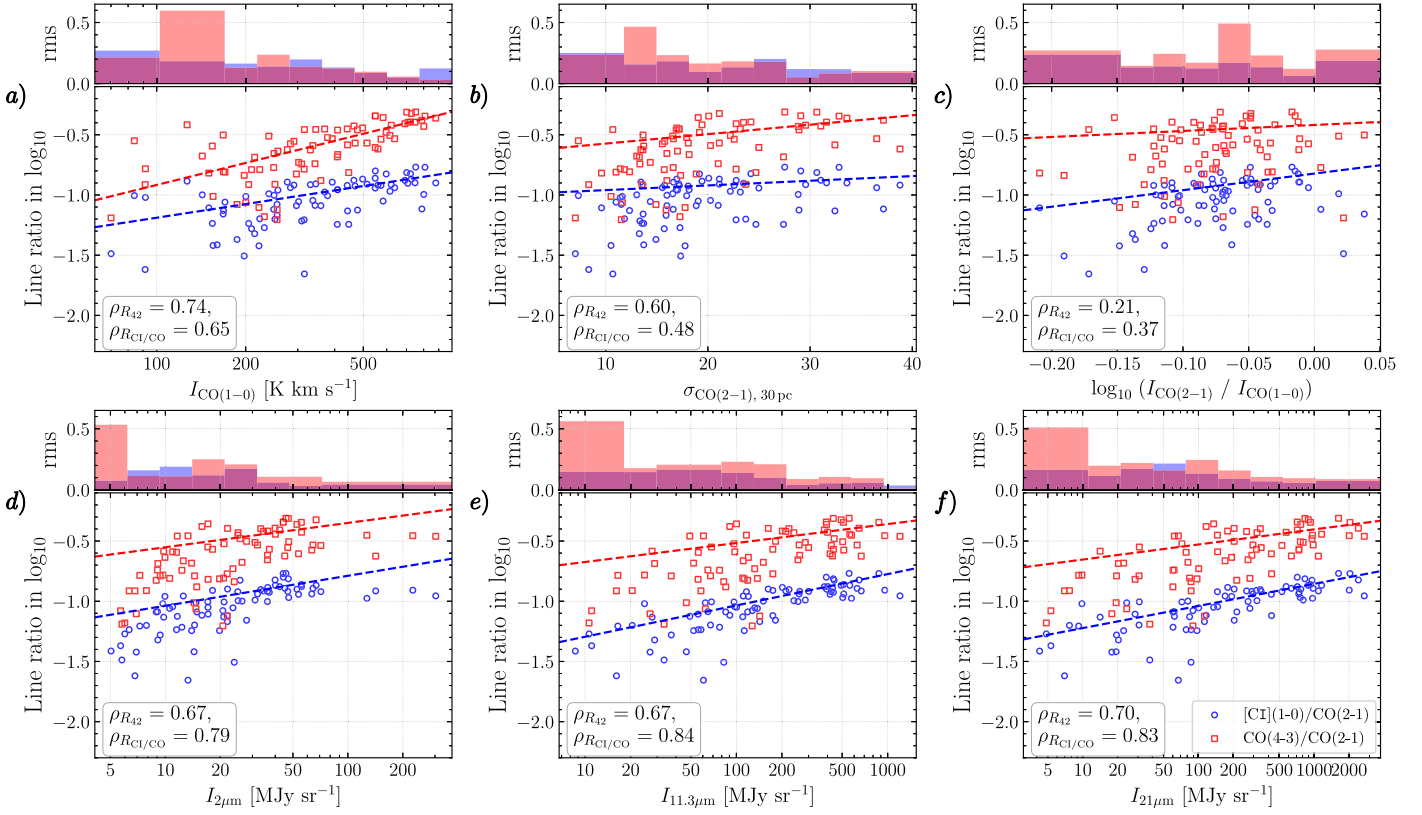
Figure 6. Panels (a)–(f): R_{42} in red and R_{CICO} in blue as functions of six variables at 330 pc resolution across the inner part of NGC 1365: (a) CO (1–0) line-integrated intensity, (b) velocity dispersion, (c) R_{21} line ratio, (d) 2, (e) 11.3, and (f) 21 μm emission. Dashed lines are the best-fit trends and legends show the Spearman's rank correlation coefficients, which are also reported in Table 1. Each inset upper panel shows the rms distribution of the data after subtracting the best-fit trend in bins of the horizontal-axis variable.

Gao et al. 2021), it shows only moderately excited CO and C I. As shown in the next section, the center's line ratios tracing CO excitation and dissociation are consistent with other regions when correlating these line ratios with mid-IR emission. At our resolution, we do not find any evidence of an extreme XDR such as a highly excited CO SLED, as seen in, for example, Mrk 231 (van der Werf et al. 2010), NGC 1068 (Spinoglio et al. 2012), and other local ultra-luminous infrared galaxies whose global R_{41} are highly excited or even close to being thermalized ($\sim$0.85–1.1; see also Rangwala et al. 2011; Meijerink et al. 2013; Kamenetzky et al. 2014; Glenn et al. 2015; Liu et al. 2015; Rosenberg et al. 2015; Kamenetzky et al. 2016, 2017; Lu et al. 2017). We observe $I_{[CI](1-0)}/I_{CO(1-0)} = 0.10$ and $I_{[CI](1-0)}/I_{CO(2-1)} = 0.11$ in NGC 1365's center at 330 pc resolution. The fitted [CI/CO] is $0.25^{+0.23}_{-0.01}$ (Table 2). These line ratios and abundance ratio are much lower than those measured in the more powerful AGNs in NGC 7469 (Izumi et al. 2020) and NGC 1068 (Saito et al. 2022a, 2022b), which have $I_{[CI](1-0)}/I_{CO(1-0)} \sim 0.5$–1 and [CI/CO] $\gtrsim$ 1.

3.3. Correlations of CO and C I Line Ratios

We investigate what star formation and ISM properties correlate with the CO and C I line ratios in Figure 6. We examine CO (1–0) line-integrated intensity ($I_{CO(1-0)}$), molecular gas velocity dispersion ($\sigma_{CO(2-1),30pc}$[43]), R_{21}, 21 μm, PAH-dominated 11.3 μm, and

stellar-continuum-dominated 2 μm intensities, all at PSF-matched 3″.5 ($\sim$330 pc) resolution and sampled in independent resolution units (by binning in hexagons with diameter equaling the beam FWHM 3″.5, then taking the aperture center value). For each pair of variables, we perform a linear fitting in log–log space with the `scipy.optimize.curve_fit` code, including errors on the line ratios propagated from the original moment and uncertainty maps (Section 2.2). We obtain a best-fit slope, N, and intercept, A, for each fit and calculate the rms of the data points around the best-fitting line. We also calculate the Spearman's correlation coefficient, ρ, and null hypothesis probability, P_0, using the `pingouin` code. The resulting parameters are summarized in Table 1.

The properties that correlate the most strongly with R_{42} and R_{CICO} are the PAH-dominated 11.3 μm, the dust-continuum-dominated 21 μm, and the stellar-continuum-dominated 2 μm emission, with $\rho > 0.7$. The $I_{CO(1-0)}$ is the next strongly correlated variable. The velocity dispersion, $\sigma_{CO(2-1),30pc}$, and R_{21} show weak or no correlation, with $\rho \lesssim 0.3$.

For each scatter plot panel in Figure 6, we show the rms distribution of the data in bins of the horizontal-axis variable. In all cases (except for R_{21}, panel (c)) the rms is higher at lower x-axis values. For all variables except $I_{CO(1-0)}$ (panel (a)), R_{42} and R_{CICO} tend to lie below the fitted line at the faint end. In regions with low CO intensities, the CO (4–3) line can still be as highly excited as the CO-brightest regions, despite a factor of $\sim$10 weaker CO (1–0) emission. This may be surprising if the CO (1–0) emission indeed indicates lower gas surface density and perhaps volume density, but these regions might also simply show low CO (1–0) at 330 pc resolution because of

---

[43] For the molecular gas velocity dispersion, we use the native-resolution CO (2–1) equivalent width map (Schinnerer et al. 2023) then compute the average in apertures with size equaling the common resolution, so as to trace the velocity dispersion at $\sim$30 pc.

Table 1
Linear Fitting and Statistical Parameters for the Line Ratio Correlations

x variable	$\log_{10} I_{[\mathrm{C\,I}](1-0)}/I_{\mathrm{CO}(2-1)}$					$\log_{10} I_{\mathrm{CO}(4-3)}/I_{\mathrm{CO}(2-1)}$				
	N	A	ρ	P_0	rms	N	A	ρ	P_0	rms
(1) $\log_{10} I_{\mathrm{CO}(1-0)}$	0.38	−1.94	0.65	<0.001	0.16	0.61	−2.13	0.74	<0.001	0.25
(2) $\sigma_{\mathrm{CO}(2-1),\,30\,\mathrm{pc}}$	0.00	−1.00	0.48	<0.001	0.19	0.01	−0.65	0.60	<0.001	0.28
(3) $\log_{10}(I_{\mathrm{CO}(2-1)}/I_{\mathrm{CO}(1-0)})$	1.38	−0.82	0.37	0.001	0.18	0.50	−0.42	0.21	0.064	0.30
(4) $\log_{10} I_{2\,\mu m}$	0.25	−1.29	0.79	<0.001	0.15	0.20	−0.75	0.67	<0.001	0.27
(5) $\log_{10} I_{11.3\,\mu m}$	0.26	−1.56	0.84	<0.001	0.12	0.16	−0.83	0.67	<0.001	0.26
(6) $\log_{10} I_{21\,\mu m}$	0.18	−1.41	0.83	<0.001	0.13	0.13	−0.78	0.70	<0.001	0.25

Notes. Best-fit Slope N and Intercept A of the $y = N \cdot x + A$ Lines Shown in Figure 6, where y is One of the $\log_{10} R_{\mathrm{CICO}} \equiv \log_{10}(I_{[\mathrm{C\,I}](1-0)}/I_{\mathrm{CO}(2-1)})$ and $\log_{10} R_{42} \equiv \log_{10}(I_{\mathrm{CO}(4-3)}/I_{\mathrm{CO}(2-1)})$ Line Ratios, and x is One of the Variables to Correlate with: (1) the CO (1–0) Integrated Intensity $\log_{10} I_{\mathrm{CO}(1-0)}$; (2) the High-resolution (~30 pc) CO (2–1) Moment-2 map, Convolved to the 3″5 (~330 pc) Resolution $\sigma_{\mathrm{CO}(2-1),\,30\,\mathrm{pc}}$; (3) the Low-$J$ CO Line Ratio $\log_{10}(I_{\mathrm{CO}(2-1)}/I_{\mathrm{CO}(1-0)})$; (4) the Stellar Continuum Dominated 2 μm Emission $\log_{10} I_{2\,\mu m}$; (5) the PAH Dominated 11.3 μm Emission $\log_{10} I_{11.3\,\mu m}$; and (6) the Dust Continuum Dominated 21 μm Emission $\log_{10} I_{21\,\mu m}$. For each of R_{CICO} and R_{42}, we list five fitting result parameters: the best-fit slope N, the intercept A, the Spearman's correlation coefficient ρ, the null hypothesis probability P_0, and the rms scatter of data points after subtracting the best-fit line. See Section 3.3 for details.

a low area filling fraction. Obtaining higher-resolution high-J CO and C I observations is critical to understanding these scenarios in the future.

In panel (b) of Figure 6, we find no correlations of R_{42} or R_{CICO} versus σ_{CO}, with slope ~0. This indicates that CO excitation and C I enrichment correlate more strongly with radiation properties than with gas dynamics in this starburst ring. Indeed, in Figure 1(g), we find a peak $\sigma_{\mathrm{CO}} \sim 50$ km s^{-1} at the Southern Arm, whereas the Northern Arm with the strongest star formation and most numerous YMCs has nearly half that value, i.e., $\sigma_{\mathrm{CO}} \sim 20$–30 km s^{-1}. Schinnerer et al. (2023) find that the CO emission in this system is usually composed of multiple (e.g., 2–4) line-of-sight velocity components, with individual components having a similar line width $\sigma \sim 19$ km s^{-1}. Therefore, this geometry effect may well blend out any σ_{CO} versus line ratios trends in this study.

In panel (c) of Figure 6, the poor correlation between R_{21} and R_{42} at our ~330 pc resolution indicates that the low-J and mid-J CO SLED shapes are largely decoupled. R_{21} is mostly saturated/thermalized in environments like the center of NGC 1365. It is therefore necessary to obtain higher-J CO lines to trace the CO excitation.

The stellar-continuum-dominated 2 μm, PAH-dominated 11.3 μm, and warm dust-continuum-dominated 21 μm emission all show tight, positive correlations with the line ratios, as seen in panels (d)–(f) of Figure 6. These correlations are robust (i.e., tighter than about 0.2 dex) in the range of $10 \lesssim I_{2\,\mu m}/(\mathrm{MJy\ sr}^{-1}) \lesssim 80$, $20 \lesssim I_{11.3\,\mu m}/(\mathrm{MJy\ sr}^{-1}) \lesssim 1000$, and $20 \lesssim I_{21\,\mu m}/(\mathrm{MJy\ sr}^{-1}) \lesssim 2000$, respectively. The 2 μm correlation has the smallest valid range, only less than a decade, whereas the dust correlations are valid over nearly two decades. The galaxy center and its surrounding apertures are outliers in the line ratio versus $I_{2\,\mu m}$ plot even at our ~330 pc resolution, but not for the line ratios versus PAH or dust continuum. We caution that the statistics is based on only one starburst ring system at a coarse resolution. Larger-sample studies will be critical to deeper understanding of the statistics.

Comparing the trends in R_{42} to those in R_{CICO}, we find similar correlations relating each line ratio to the other variables. The trends with R_{CICO} do tend to be tighter, with scatter about ~0.05–0.1 dex smaller than we find for R_{42}. This likely relates to the fact that [C I] (1–0) has a >30× lower critical density and 2× lower upper-level energy temperature (E_u) than CO (4–3) (e.g., Crocker et al. 2019, Table 3). This

makes [C I] (1–0) more sensitive to the temperature and low-density part of the medium, which is substantially affected by the stellar feedback from embedded star formation traced by the YMCs, PAH emission, and warm dust continuum.

4. Summary

In this Letter we use multi-J CO and C I line ratios to trace the CO excitation and dissociation and infer molecular gas temperature, density, and feedback under the impact of YMCs in the bar-fed starbursting ring of NGC 1365. The mid-J CO SLED up to CO (4–3), and the [C I] (1–0) line, together with the distribution of young (<10 Myr), massive ($M_\star \gtrsim 10^6\,M_\odot$) star clusters revealed by JWST allow us to infer how the molecular gas properties are impacted by stellar feedback from YMCs as the gas enters and circulates in the starburst ring. We summarize our findings below.

1. The Northern and Southern arms have a high molecular gas density, relatively low temperature and [CI/CO] abundance ratio, with observed line ratios $R_{21} \sim 0.8$–1, $R_{42} \sim 0.45$–0.51, and $R_{\mathrm{CICO}} \sim 0.1$–0.2. These are in line with the scenario where the Northern and Southern arm regions are the locations where molecular gas flows into the starburst ring along the bar and dust lanes. Bar-induced shocks may play a key role in affecting the gas there, but further observational support is needed.

2. The molecular gas in the Mid-Southwest region seems largely impacted by the stellar feedback (i.e., low R_{42} but high R_{21} and R_{CICO}), exhibiting a low gas density ($\log(n_{\mathrm{H}_2}/\mathrm{cm}^{-3}) \sim 2.9$), high temperature (~100 K), and enhanced [CI/CO] abundance ratio ($\gtrsim 1$) compared to the upstream Northern Arm ($\log(n_{\mathrm{H}_2}/\mathrm{cm}^{-3}) \sim 3.4$, $T_{\mathrm{kin}} \sim 40$ K, and [CI/CO] ~ 0.7) as inferred from our LVG fitting.

3. The molecular gas in the Mid-East region exhibits both a high R_{42} and R_{CICO}, possibly due to its much higher density than that of the Mid-Southwest region ,and thus being less impacted by the stellar feedback. Our LVG fitting infer that there is only a moderate decrease in gas density ($\log(n_{\mathrm{H}_2}/\mathrm{cm}^{-3}) \sim 3.4$) or weak increase in temperature (~25 K) and [CI/CO] (~0.5) compared to the upstream Southern Arm region ($\log(n_{\mathrm{H}_2}/\mathrm{cm}^{-3}) \sim 4.0$, $T_{\mathrm{kin}} \sim 15$ K, and [CI/CO] ~ 0.2).

4. Through a correlation analysis, we find that the mid-J CO excitation R_{42} or the CO dissociation tracer R_{CICO} do not

obviously correlate with the low-J CO excitation R_{21}, likely because the R_{21} shows high ratios and appears nearly thermalized across the whole region. We also find little correlation between the line ratios and the apparent CO line velocity dispersion, implying that the complex gas dynamics does not affect the CO excitation and photo-dissociation in the starburst ring.

5. We find tightest correlations between R_{42} or R_{CICO} and the mid-IR PAH-dominated 11.3 μm and dust-continuum-dominated 21 μm emission ($\rho \sim 0.67$–0.84, rms ~ 0.12–0.27 dex). The stellar-continuum-dominated 2 μm emission correlates with R_{42} and R_{CICO} well, too ($\rho \sim 0.67$–0.79, rms ~ 0.15–0.27 dex), but the very center does not follow the trend.

6. The R_{CICO} correlations with mid-IR dust/PAH and near-IR stellar emission properties are in general slightly tighter (~ 0.1 higher in ρ) and less scattered (~ -0.5 dex smaller rms) than those of R_{42}. This may relate to the significantly lower critical density of [C I] (1–0) than CO (4–3) and to CO dissociation, which makes C I more sensitive to the mid-IR-traced bulk of star-forming gas and stellar feedback.

7. Despite hosting a Seyfert 1.5 AGN and having an ionized gas outflow, NGC 1365's central ~ 330 pc area (our resolution unit) exhibits only moderate CO excitation and C I/CO line ratio, comparable to or even less highly excited than other regions that we studied.

Software: Astropy (Astropy Collaboration et al. 2013, 2018, 2022), CASA software (the CASA Team et al. 2022), Matplotlib (Hunter 2007), MICHI2 (Liu 2020; Liu et al. 2021), PHANGS–ALMA pipeline (Leroy et al. 2021b), Photutils (Bradley et al. 2020), RADEX (van der Tak et al. 2007), Scipy (Virtanen et al. 2020), spectral_cube (Ginsburg et al. 2019).

Appendix
LVG Model Fitting

We illustrate our Monte Carlo LVG model fitting in Figure A1. We first use RADEX (van der Tak et al. 2007)

with the Leiden Atomic and Molecular Database (Schoier et al. 2005) to build a library of LVG models with the parameter grids as described in Section 3.2. Then, we use the MICHI2 code (Liu et al. 2021) to run Monte Carlo fitting and obtain the $1/\chi^2$ posterior distribution for each parameter (following the statistical criterion of $\pm 1\sigma$ in Press et al. 1992). Blue squares with error bars are the CO and C I line fluxes to be fitted, and black to gray dots are model data points with different reduced χ^2. Our free model parameters are $\log n_{H_2}$, T_{kin}, [CI/CO], and normalization (beam-filling factor). Their $1/\chi^2$ distributions and the $\pm 1\sigma$ ranges are shown in the lower panels. All fitting results are presented in Table 2.
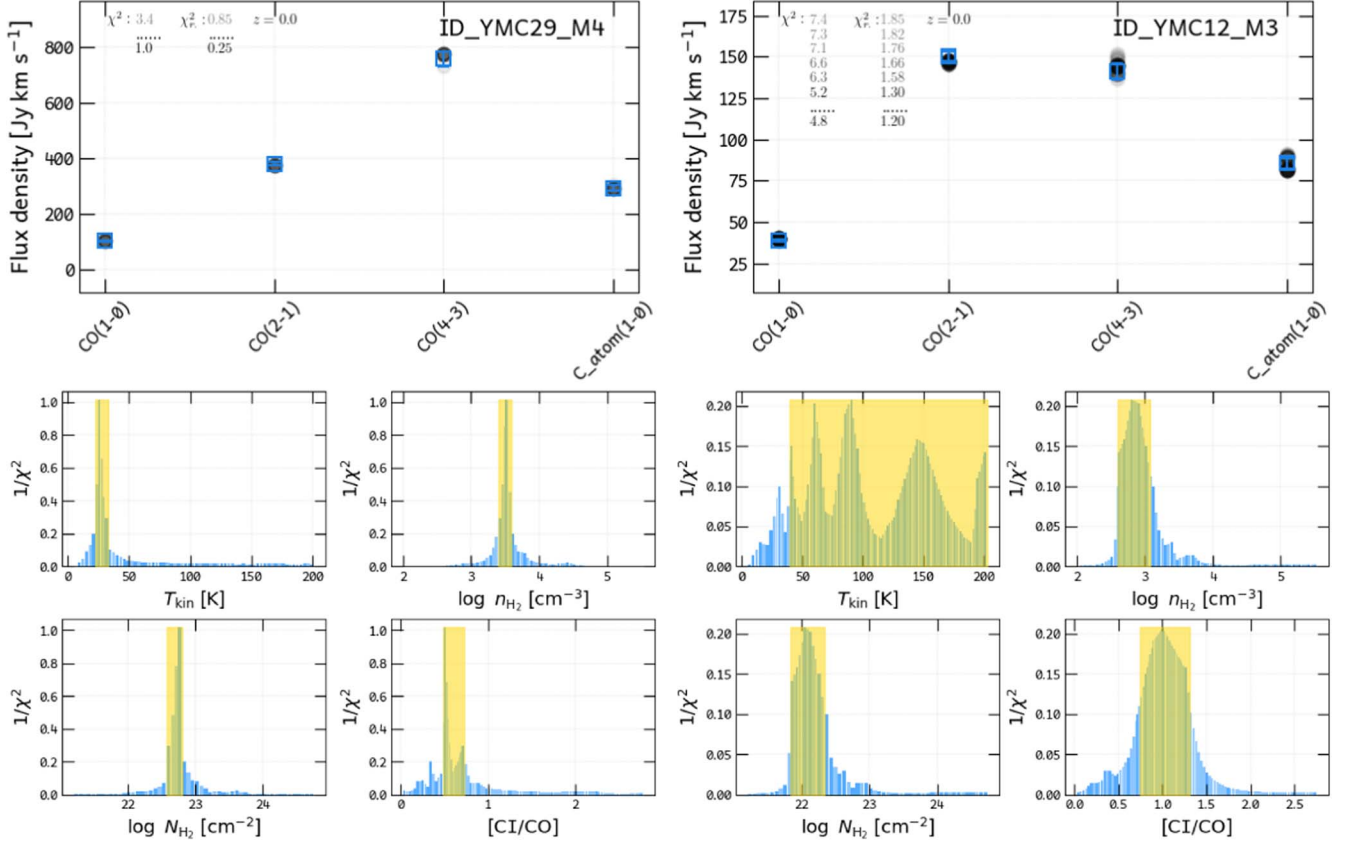
Figure A1. Upper row: the CO and C I SLED of YMC 29 (M4, the most-excited YMC aperture in the Northern Arm; left panel) and that of YMC 12 (M3, the least-excited YMC aperture in the Mid-Southwest region; right panel). Observed line fluxes are shown as blue squares with error bars. Black to gray solid circles are fitted points from a series of fitting within 1σ with an increasing χ^2 (and reduced χ^2, χ_r^2). Bottom panels: corresponding $1/\chi^2$ distributions of model fitting parameters T_{kin}, $\log n_{H_2}$, $\log N_{H_2}$ (nonindependent) and [CI/CO] from the MICHI2 code. Yellow shading indicates the $\pm 1\sigma$ parameter range.

Table 2
Results of MICHI2 LVG Fitting to the CO and C I SLED of YMC, CO Peak, and Galaxy Center Apertures

Aperture	R.A. (J2000)	Decl. (J2000)	$\log n_{H_2}/cm^{-3}$	$\log N_{H_2}/cm^{-2}$	T_{kin}/K	[CI/CO]
Northern Arm						
CO.N2	53.40340917	−36.13729972	$3.20^{+0.25}_{-0.12}$	$22.44^{+0.26}_{-0.12}$	$25.0^{+8.0}_{-11.2}$	$0.60^{+0.13}_{-0.25}$
36	53.40311543	−36.13715197	$2.70^{+0.35}_{-0.02}$	$21.94^{+0.36}_{-0.01}$	$155.0^{+12.9}_{-110.0}$	$1.00^{+0.09}_{-0.31}$
35	53.40306629	−36.13749402	$3.30^{+0.09}_{-0.26}$	$22.54^{+0.06}_{-0.25}$	$25.0^{+24.7}_{-2.3}$	$0.60^{+0.40}_{-0.03}$
33,M5	53.40251420	−36.13768031	$3.30^{+0.09}_{-0.13}$	$22.54^{+0.06}_{-0.16}$	$35.0^{+13.0}_{-3.4}$	$0.80^{+0.16}_{-0.08}$
30	53.40098220	−36.13841668	$3.30^{+0.09}_{-0.17}$	$22.54^{+0.06}_{-0.16}$	$35.0^{+18.0}_{-3.4}$	$0.70^{+0.29}_{-0.04}$
29,M4	53.40170236	−36.13843398	$3.50^{+0.09}_{-0.11}$	$22.74^{+0.07}_{-0.16}$	$25.0^{+8.0}_{-2.3}$	$0.50^{+0.23}_{-0.02}$
28,M6	53.40318107	−36.13847524	$3.60^{+0.09}_{-0.25}$	$22.84^{+0.07}_{-0.20}$	$15.0^{+12.9}_{-1.2}$	$0.30^{+0.36}_{-0.03}$
25	53.40092801	−36.13910029	$3.40^{+0.10}_{-0.08}$	$22.64^{+0.04}_{-0.09}$	$20.0^{+2.9}_{-3.1}$	$0.40^{+0.02}_{-0.04}$
CO.N1	53.40132208	−36.13871556	$3.40^{+0.14}_{-0.05}$	$22.64^{+0.17}_{-0.06}$	$30.0^{+3.0}_{-10.2}$	$0.60^{+0.06}_{-0.20}$
Mid-Southwest Region						
22	53.40046102	−36.13984982	$3.30^{+0.02}_{-0.03}$	$22.54^{+0.01}_{-0.06}$	$20.0^{+2.9}_{-3.1}$	$0.45^{+0.03}_{-0.03}$
19	53.39952417	−36.14009082	$2.60^{+0.85}_{-0.01}$	$21.84^{+0.87}_{-0.00}$	$195.0^{+7.9}_{-180.0}$	$1.00^{+0.09}_{-0.70}$
12,M3	53.39955255	−36.14112108	$2.80^{+0.27}_{-0.20}$	$22.04^{+0.30}_{-0.20}$	$90.0^{+112.9}_{-50.6}$	$1.00^{+0.31}_{-0.25}$
11	53.39977124	−36.14112797	$2.70^{+0.35}_{-0.02}$	$21.94^{+0.36}_{-0.01}$	$175.0^{+17.9}_{-125.8}$	$1.25^{+0.12}_{-0.35}$
9	53.40018429	−36.14131523	$2.70^{+0.39}_{-0.02}$	$21.94^{+0.36}_{-0.08}$	$180.0^{+17.9}_{-130.8}$	$1.25^{+0.15}_{-0.41}$
7,M2	53.39987072	−36.14183303	$3.10^{+0.09}_{-0.42}$	$22.34^{+0.06}_{-0.41}$	$35.0^{+157.9}_{-3.4}$	$0.70^{+0.58}_{-0.07}$
5	53.40033806	−36.14207205	$3.30^{+0.04}_{-0.26}$	$22.54^{+0.06}_{-0.30}$	$20.0^{+17.4}_{-0.2}$	$0.40^{+0.30}_{-0.01}$
3,J	53.40069177	−36.14212741	$3.40^{+0.05}_{-0.08}$	$22.64^{+0.04}_{-0.09}$	$15.0^{+4.9}_{-4.0}$	$0.30^{+0.03}_{-0.03}$
Mid-East Region						
23	53.40337423	−36.13956883	$3.30^{+0.35}_{-0.04}$	$22.54^{+0.36}_{-0.03}$	$30.0^{+3.0}_{-16.1}$	$0.60^{+0.06}_{-0.36}$
21	53.40333174	−36.13986047	$3.40^{+0.14}_{-0.10}$	$22.64^{+0.17}_{-0.06}$	$25.0^{+2.9}_{-5.2}$	$0.45^{+0.14}_{-0.12}$
18	53.40339461	−36.14021144	$3.60^{+0.05}_{-0.25}$	$22.84^{+0.07}_{-0.20}$	$15.0^{+12.9}_{-1.2}$	$0.25^{+0.23}_{-0.03}$
16	53.40291154	−36.14045529	$3.40^{+0.14}_{-0.05}$	$22.64^{+0.17}_{-0.06}$	$25.0^{+4.7}_{-5.2}$	$0.45^{+0.05}_{-0.15}$
15	53.40321229	−36.14061030	$3.50^{+0.14}_{-0.06}$	$22.74^{+0.16}_{-0.05}$	$20.0^{+4.7}_{-5.0}$	$0.30^{+0.05}_{-0.10}$
13	53.40293504	−36.14082502	$3.50^{+0.09}_{-0.11}$	$22.74^{+0.07}_{-0.10}$	$20.0^{+7.9}_{-3.2}$	$0.30^{+0.18}_{-0.00}$
10	53.40283403	−36.14127466	$3.60^{+0.05}_{-0.23}$	$22.84^{+0.07}_{-0.25}$	$15.0^{+14.7}_{-1.2}$	$0.20^{+0.30}_{+0.00}$
Southern Arm						
1	53.40028097	−36.14257775	$3.50^{+0.05}_{-0.05}$	$22.74^{+0.00}_{-0.06}$	$15.0^{+4.9}_{-1.1}$	$0.25^{+0.02}_{-0.01}$
2	53.39989135	−36.14257526	$3.50^{+0.04}_{-0.11}$	$22.74^{+0.07}_{-0.10}$	$15.0^{+7.9}_{-1.2}$	$0.25^{+0.13}_{-0.01}$
CO.S1	53.39917000	−36.14308806	$4.10^{+0.04}_{-0.01}$	$23.34^{+0.06}_{-0.01}$	$10.0^{+3.9}_{-2.0}$	$0.05^{+0.01}_{-0.02}$
CO.S2	53.39845708	−36.14325417	$4.00^{+0.05}_{-0.05}$	$23.24^{+0.03}_{-0.04}$	$10.0^{+1.0}_{-2.0}$	$0.05^{+0.01}_{-0.02}$
CO.S3	53.39761333	−36.14309889	$3.50^{+0.05}_{-0.09}$	$22.74^{+0.00}_{-0.06}$	$15.0^{+4.9}_{-1.1}$	$0.15^{+0.03}_{-0.03}$
Center						
Center	53.40154167	−36.14041694	$3.50^{+0.04}_{-0.24}$	$22.74^{+0.07}_{-0.23}$	$15.0^{+12.9}_{-1.2}$	$0.25^{+0.23}_{-0.01}$

Note. YMC IDs and R.A. and decl. coordinates are from Whitmore et al. (2023). See description of the fitting in Section 3.2. See also Figure 5 for the illustration of the fitted parameters along the starburst ring.

ORCID iDs

Daizhong Liu https://orcid.org/0000-0001-9773-7479
Eva Schinnerer https://orcid.org/0000-0002-3933-7677
Yixian Cao https://orcid.org/0000-0001-5301-1326
Adam Leroy https://orcid.org/0000-0002-2545-1700
Antonio Usero https://orcid.org/0000-0003-1242-505X
Erik Rosolowsky https://orcid.org/0000-0002-5204-2259
J. M. Diederik Kruijssen https://orcid.org/0000-0002-8804-0212
Mélanie Chevance https://orcid.org/0000-0002-5635-5180
Simon C. O. Glover https://orcid.org/0000-0001-6708-1317
Mattia C. Sormani https://orcid.org/0000-0001-6113-6241
Alberto D. Bolatto https://orcid.org/0000-0002-5480-5686
Jiayi Sun https://orcid.org/0000-0003-0378-4667
Sophia K. Stuber https://orcid.org/0000-0002-9333-387X
Yu-Hsuan Teng https://orcid.org/0000-0003-4209-1599
Frank Bigiel https://orcid.org/0000-0003-0166-9745

Ivana Bešlić https://orcid.org/0000-0003-0583-7363
Kathryn Grasha https://orcid.org/0000-0002-3247-5321
Jonathan D. Henshaw https://orcid.org/0000-0001-9656-7682
Ashley T. Barnes https://orcid.org/0000-0003-0410-4504
Jakob S. den Brok https://orcid.org/0000-0002-8760-6157
Toshiki Saito https://orcid.org/0000-0001-9016-2641
Daniel A. Dale https://orcid.org/0000-0002-5782-9093
Elizabeth J. Watkins https://orcid.org/0000-0002-7365-5791
Hsi-An Pan https://orcid.org/0000-0002-1370-6964
Ralf S. Klessen https://orcid.org/0000-0002-0560-3172
Eric Emsellem https://orcid.org/0000-0002-6155-7166
Gagandeep S. Anand https://orcid.org/0000-0002-5259-2314
Sinan Deger https://orcid.org/0000-0003-1943-723X
Oleg V. Egorov https://orcid.org/0000-0002-4755-118X

Christopher M. Faesi ⓘ https://orcid.org/0000-0001-5310-467X
Hamid Hassani ⓘ https://orcid.org/0000-0002-8806-6308
Kirsten L. Larson ⓘ https://orcid.org/0000-0003-3917-6460
Janice C. Lee ⓘ https://orcid.org/0000-0002-2278-9407
Laura A. Lopez ⓘ https://orcid.org/0000-0002-1790-3148
Jérôme Pety ⓘ https://orcid.org/0000-0003-3061-6546
Karin Sandstrom ⓘ https://orcid.org/0000-0002-4378-8534
David A. Thilker ⓘ https://orcid.org/0000-0002-8528-7340
Bradley C. Whitmore ⓘ https://orcid.org/0000-0002-3784-7032
Thomas G. Williams ⓘ https://orcid.org/0000-0002-0012-2142

References

Anand, G. S., Lee, J. C., Van Dyk, S. D., et al. 2021b, MNRAS, 501, 3621
Anand, G. S., Rizzi, L., Tully, R. B., et al. 2021a, AJ, 162, 80
Astropy Collaboration, Price-Whelan, A. M., Lim, P. L., et al. 2022, ApJ, 935, 167
Astropy Collaboration, Price-Whelan, A. M., Sipőcz, B. M., et al. 2018, AJ, 156, 123
Astropy Collaboration, Robitaille, T. P., Tollerud, E. J., et al. 2013, A&A, 558, A33
Athanassoula, E. 1992, MNRAS, 259, 345
Audibert, A., Combes, F., García-Burillo, S., et al. 2019, A&A, 632, A33
Barnes, A. T., Chandar, R., Kreckel, K., et al. 2022, A&A, 662, L6
Barnes, A. T., Glover, S. C. O., Kreckel, K., et al. 2021, MNRAS, 508, 5362
Bayet, E., Gerin, M., Phillips, T. G., & Contursi, A. 2004, A&A, 427, 45
Bayet, E., Gerin, M., Phillips, T. G., & Contursi, A. 2006, A&A, 460, 467
Bradley, L., Sipőcz, B., Robitaille, T., et al. 2020, astropy/photutils: 1.0.0, Zenodo, doi:10.5281/zenodo.4044744
Buta, R., & Combes, F. 1996, FCPh, 17, 95
Calzetti, D., Lee, J. C., Sabbi, E., et al. 2015, AJ, 149, 51
Chevance, M., Kruijssen, J. M. D., Hygate, A. P. S., et al. 2020, MNRAS, 493, 2872
Chevance, M., Krumholz, M. R., McLeod, A. F., et al. 2022, arXiv:2203.09570
Cicone, C., Brusa, M., Ramos Almeida, C., et al. 2018, NatAs, 2, 176
Combes, F., García-Burillo, S., Audibert, A., et al. 2019, A&A, 623, A79
Crocker, A. F., Pellegrini, E., Smith, J.-D. T., et al. 2019, ApJ, 887, 105
Curran, S. J., Polatidis, A. G., Aalto, S., & Booth, R. S. 2001, A&A, 368, 824
de Jong, T., Boland, W., & Dalgarno, A. 1980, A&A, 91, 68
Emsellem, E., Schinnerer, E., Santoro, F., et al. 2022, A&A, 659, A191
Erroz-Ferrer, S., Carollo, C. M., den Brok, M., et al. 2019, MNRAS, 484, 5009
Fazeli, N., Busch, G., Valencia-S., M., et al. 2019, A&A, 622, A128
Fukui, Y., Torii, K., Ohama, A., et al. 2016, ApJ, 820, 26
Gadotti, D. A., Sánchez-Blázquez, P., Falcón-Barroso, J., et al. 2019, MNRAS, 482, 506
Galliano, E., Alloin, D., Pantin, E., et al. 2008, A&A, 492, 3
Galliano, E., Alloin, D., Pantin, E., Lagage, P. O., & Marco, O. 2005, A&A, 438, 803
Gao, Y., Egusa, F., Liu, G., et al. 2021, ApJ, 913, 139
García-Burillo, S., Alonso-Herrero, A., Ramos Almeida, C., et al. 2021, A&A, 652, A98
García-Burillo, S., Usero, A., Fuente, A., et al. 2010, A&A, 519, A2
Ginsburg, A., Koch, E., Robitaille, T., et al. 2019, radio-astro-tools/spectral-cube: v0.4.4, Zenodo, doi:10.5281/zenodo.2573901
Glenn, J., Rangwala, N., Maloney, P. R., & Kamenetzky, J. R. 2015, ApJ, 800, 105
Goldreich, P., & Kwan, J. 1974, ApJ, 189, 441
Grasha, K., Calzetti, D., Bittle, L., et al. 2018, MNRAS, 481, 1016
Greve, T. R., Leonidaki, I., Xilouris, E. M., et al. 2014, ApJ, 794, 142
Harrison, C. M., Costa, T., Tadhunter, C. N., et al. 2018, NatAs, 2, 198
Henshaw, J. D., Ginsburg, A., Haworth, T. J., et al. 2019, MNRAS, 485, 2457
Henshaw, J. D., Longmore, S. N., Kruijssen, J. M. D., et al. 2016, MNRAS, 457, 2675
Hjelm, M., & Lindblad, P. O. 1996, A&A, 305, 727
Hollenbach, D. J., Takahashi, T., & Tielens, A. G. G. M. 1991, ApJ, 377, 192
Hollenbach, D. J., & Tielens, A. G. G. M. 1997, ARA&A, 35, 179
Hunter, J. D. 2007, CSE, 9, 90

Israel, F. P., Rosenberg, M. J. F., & van der Werf, P. 2015, A&A, 578, A95
Israel, F. P., White, G. J., & Baas, F. 1995, A&A, 302, 343
Izumi, T., Nguyen, D. D., Imanishi, M., et al. 2020, ApJ, 898, 75
Jorsater, S., & van Moorsel, G. A. 1995, AJ, 110, 2037
Kamenetzky, J., Rangwala, N., & Glenn, J. 2017, MNRAS, 471, 2917
Kamenetzky, J., Rangwala, N., Glenn, J., Maloney, P. R., & Conley, A. 2014, ApJ, 795, 174
Kamenetzky, J., Rangwala, N., Glenn, J., Maloney, P. R., & Conley, A. 2016, ApJ, 829, 93
Kaufman, M. J., Wolfire, M. G., Hollenbach, D. J., & Luhman, M. L. 1999, ApJ, 527, 795
Kelly, G., Viti, S., García-Burillo, S., et al. 2017, A&A, 597, A11
Kennicutt, R. C., & Evans, N. J. 2012, ARA&A, 50, 531
Kim, J., Chevance, M., Kruijssen, J. M. D., et al. 2022, MNRAS, 516, 3006
Kristen, H., Jorsater, S., Lindblad, P. O., & Boksenberg, A. 1997, A&A, 328, 483
Kruijssen, J. M. D., Schruba, A., Chevance, M., et al. 2019, Natur, 569, 519
Langer, W. 1976, ApJ, 206, 699
Lee, J. C., Whitmore, B. C., Thilker, D. A., et al. 2022, ApJS, 258, 10
Lee, J., Sandstrom, S. M., Leroy, A. K., et al. 2023, ApJL, 944, L17
Lena, D., Robinson, A., Storchi-Bergmann, T., et al. 2016, MNRAS, 459, 4485
Leroy, A. K., Hughes, A., Liu, D., et al. 2021b, ApJS, 255, 19
Leroy, A. K., Schinnerer, E., Hughes, A., et al. 2021a, ApJS, 257, 43
Lindblad, P. O. 1999, A&ARv, 9, 221
Liu, D. 2020, michi2: SED and SLED fitting tool, Astrophysics Source Code Library, record ascl:2005.002
Liu, D., Daddi, E., Schinnerer, E., et al. 2021, ApJ, 909, 56
Liu, D., Gao, Y., Isaak, K., et al. 2015, ApJL, 810, L14
Liu, D., Schinnerer, E., Saito, T., et al. 2022, arXiv:2212.09661
Lu, N., Zhao, Y., Díaz-Santos, T., et al. 2017, ApJS, 230, 1
Maciejewski, W., Teuben, P. J., Sparke, L. S., & Stone, J. M. 2002, MNRAS, 329, 502
Maloney, P. R., Hollenbach, D. J., & Tielens, A. G. G. M. 1996, ApJ, 466, 561
Meier, D. S., Walter, F., Bolatto, A. D., et al. 2015, ApJ, 801, 63
Meijerink, R., Kristensen, L. E., Weiß, A., et al. 2013, ApJL, 762, L16
Meijerink, R., & Spaans, M. 2005, A&A, 436, 397
Meijerink, R., Spaans, M., & Israel, F. P. 2007, A&A, 461, 793
Morganti, R., Tsvetanov, Z. I., Gallimore, J., & Allen, M. G. 1999, A&AS, 137, 457
Pan, H.-A., Schinnerer, E., Hughes, A., et al. 2022, ApJ, 927, 9
Papadopoulos, P. P. 2010, ApJ, 720, 226
Papadopoulos, P. P., Bisbas, T. G., & Zhang, Z.-Y. 2018, MNRAS, 478, 1716
Papadopoulos, P. P., Isaak, K. G., & van der Werf, P. P. 2007, ApJ, 668, 815
Papadopoulos, P. P., Thi, W.-F., Miniati, F., & Viti, S. 2011, MNRAS, 414, 1705
Papadopoulos, P. P., van der Werf, P., Isaak, K., & Xilouris, E. M. 2010, ApJ, 715, 775
Pastras, S., Patsis, P. A., & Athanassoula, E. 2022, Univ, 8, 290
Phillips, M. M., Turtle, A. J., Edmunds, M. G., & Pagel, B. E. J. 1983, MNRAS, 203, 759
Press, W. H., Teukolsky, S. A., Vetterling, W. T., & Flannery, B. P. 1992, Numerical recipes in C. The art of scientific computing (2nd ed.; Cambridge: Cambridge Univ. Press)
Rangwala, N., Maloney, P. R., Glenn, J., et al. 2011, ApJ, 743, 94
Rosenberg, M. J. F., van der Werf, P. P., Aalto, S., et al. 2015, ApJ, 801, 72
Rosolowsky, E., Hughes, A., Leroy, A. K., et al. 2021, MNRAS, 502, 1218
Rosolowsky, E., & Leroy, A. 2006, PASP, 118, 590
Saito, T., Takano, S., Harada, N., et al. 2022a, ApJL, 927, L32
Saito, T., Takano, S., Harada, N., et al. 2022b, ApJ, 935, 155
Sakamoto, K., Ho, P. T. P., Mao, R.-Q., Matsushita, S., & Peck, A. B. 2007, ApJ, 654, 782
Salak, D., Nakai, N., Seta, M., & Miyamoto, Y. 2019, ApJ, 887, 143
Sandqvist, A., Joersaeter, S., & Lindblad, P. O. 1995, A&A, 295, 585
Schinnerer, E., Emsellem, E., Henshaw, J., et al. 2023, ApJL, 944, L15
Schoier, F. L., van der Tak, F. F. S., van Dishoeck, E. F., & Black, J. H. 2005, A&A, 432, 369
Scoville, N. Z. 2013, in Secular Evolution of Galaxies, ed. J. Falcón-Barroso & J. H. Knapen (Cambridge: Cambridge Univ. Press), 491
Sellwood, J. A., & Masters, K. L. 2022, ARA&A, 60
Sellwood, J. A., & Wilkinson, A. 1993, RPPh, 56, 173
Shirley, Y. L. 2015, PASP, 127, 299
Spinoglio, L., Pereira-Santaella, M., Busquet, G., et al. 2012, ApJ, 758, 108
Sun, J., Leroy, A. K., Schinnerer, E., et al. 2020, ApJL, 901, L8
Tacconi, L. J., Genzel, R., & Sternberg, A. 2020, ARA&A, 58, 157
The CASA Team, Bean, B., Bhatnagar, S., et al. 2022, PASP, 134, 114501

Tielens, A. G. G. M., & Hollenbach, D. 1985a, ApJ, 291, 722
Tielens, A. G. G. M., & Hollenbach, D. 1985b, ApJ, 291, 747
Turner, T. J., Urry, C. M., & Mushotzky, R. F. 1993, ApJ, 418, 653
Usero, A., García-Burillo, S., Martín-Pintado, J., Fuente, A., & Neri, R. 2006, A&A, 448, 457
van der Tak, F. F. S., Black, J. H., Schöier, F. L., Jansen, D. J., & van Dishoeck, E. F. 2007, A&A, 468, 627
van der Werf, P. P., Isaak, K. G., Meijerink, R., et al. 2010, A&A, 518, L42

Venturi, G., Nardini, E., Marconi, A., et al. 2018, A&A, 619, A74
Veron, P., Lindblad, P. O., Zuiderwijk, E. J., Veron, M. P., & Adam, G. 1980, A&A, 87, 245
Virtanen, P., Gommers, R., Oliphant, T. E., et al. 2020, NatMe, 17, 261
Weiß, A., Downes, D., Neri, R., et al. 2007, A&A, 467, 955
Whitmore, B., Chandar, R., Rodriguez, J., et al. 2023, ApJL, 944, L14
Wolfire, M. G., Vallini, L., & Chevance, M. 2022, ARA&A, 60, 247
Zhang, Z.-Y., Henkel, C., Gao, Y., et al. 2014, A&A, 568, A122